Inorganic Chemistry

Article

pubs.acs.org/IC

Nonstoichiometric Control of Tunnel-Filling Order, Thermal Expansion, and Dielectric Relaxation in Tetragonal Tungsten Bronzes $Ba_{0.5-x}TaO_{3-x}$

Fengjuan Pan,[†] Xiaohui Li,[‡] Fengqi Lu,[‡] Xiaoming Wang,[§] Jiang Cao,[†] Xiaojun Kuang,*[,‡,†] Emmanuel Véron,[∥,¶] Florence Porcher,[⊥] Matthew R. Suchomel,[#] Jing Wang,[†] and Mathieu Allix*[,∥,¶]

[†]MOE Key Laboratory of Bioinorganic and Synthetic Chemistry, State Key Laboratory of Optoelectronic Materials and Technologies, School of Chemistry and Chemical Engineering, Sun Yat-Sen University, Guangzhou, Guangdong 510275, P. R. China

[‡]Guangxi Ministry-Province Jointly-Constructed Cultivation Base for State Key Laboratory of Processing for Nonferrous Metal and Featured Materials, Guangxi University Key Laboratory of Nonferrous Metal Oxide Electronic Functional Materials and Devices, College of Materials Science and Engineering, Guilin University of Technology, Guilin, Guangxi 541004, P. R. China

[§]Beijing National Laboratory for Molecular Sciences, The State Key Laboratory of Rare Earth Materials Chemistry and Applications, College of Chemistry and Molecular Engineering, Peking University, Beijing 100871, P. R. China

[∥]CNRS, CEMHTI UPR 3079, Univ. Orléans, F-45071 Orléans, France

[¶]Université d'Orléans, Faculté des Sciences, Avenue du Parc Floral, Orléans 45067 Cedex 2, France

[⊥]CEA Saclay, Laboratoire Léon Brillouin, F-91191 Gif Sur Yvette, Paris, France

[#]Advanced Photon Source, Argonne National Laboratory, Lemont, Illinois 60439, United States

Supporting Information

ABSTRACT: Ordering of interpolated Ba^{2+} chains and alternate Ta−O rows $(TaO)^{3+}$ in the pentagonal tunnels of tetragonal tungsten bronzes (TTB) is controlled by the nonstoichiometry in the highly nonstoichiometric $Ba_{0.5-x}TaO_{3-x}$ system. In $Ba_{0.22}TaO_{2.72}$, the filling of Ba^{2+} and $(TaO)^{3+}$ groups is partially ordered along the *ab*-plane of the simple TTB structure, resulting in a $\sqrt{2}$-type TTB superstructure (*Pbmm*), while in $Ba_{0.175}TaO_{2.675}$, the pentagonal tunnel filling is completely ordered along the *b*-axis of the simple TTB structure, leading to a triple TTB superstructure ($P2_12_12$). Both superstructures show completely empty square tunnels favoring Ba^{2+} conduction and feature unusual accommodation of Ta^{5+} cations in the small triangular tunnels. In contrast with stoichiometric $Ba_6GaTa_9O_{30}$, which shows linear thermal expansion of the cell parameters and monotonic decrease of permittivity with temperature within 100−800 K, these TTB superstructures and slightly nonstoichiometric simple TTB $Ba_{0.4}TaO_{2.9}$ display abnormally broad and frequency-dependent extrinsic dielectric relaxations in 10^3−10^5 Hz above room temperature, a linear deviation of the *c*-axis thermal expansion around 600 K, and high dielectric permittivity ∼60−95 at 1 MHz at room temperature.

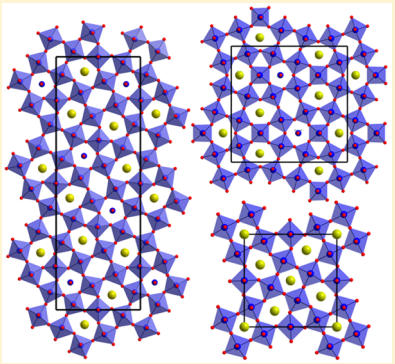

INTRODUCTION

As a derivate from perovskite prototype, tetragonal tungsten bronze (TTB) $A_4B_2C_4M_{10}O_{30}$-type materials have received considerable attention because of their technologically relevant physical properties associated with their structural polarity, leading for example to ferroelectricity,[1−3] multiferroicity,[1] relaxor,[4,5] optical nonlinearity,[2] or unusual anisotropically thermal expansion.[6] In TTB structures, *A*, *B*, and *M*, respectively, denote pentagonal, square tunnel, and the framework octahedral sites, whereas C stands for triangle tunnel sites, which are often empty in most of the TTB materials but can be occupied by small cations such as Li^+.[7] The size match of *A* and *B* cations with the tunnels and the correlated framework octahedral distortion are responsible for the polarization of the TTB structure,[4,8] and therefore, the composition/stoichiometry-dependent physical properties of the TTB materials may be controlled by tuning the cation species and occupancies in the nonequivalent tunnel and octahedral sites as well as oxygen deficiency by atmospheric reduction or acceptor-doping.[4,5]

Recently, during the phase relationship study of the BaO−Ga_2O_3−Ta_2O_5 ternary system,[9] we identified the formation of a TTB solid solution, $Ba_{0.5-x}TaO_{3-x}$ (x = 0−0.325) at 1475K, and carried out a detailed structural investigation on this TTB solid solution.[10] The results provided new insight into how the defect chemistry of TTB structures adapts to a continuous and extensive range of both cationic and anionic stoichiometries: in

Received: May 15, 2015
Published: September 8, 2015

ACS Publications © 2015 American Chemical Society

DOI: 10.1021/acs.inorgchem.5b01098
Inorg. Chem. 2015, 54, 8978−8986

highly nonstoichiometric TTB $Ba_{0.5-x}TaO_{3-x}$ (x = 0.25−0.325), the square tunnels are empty and distinct Ba^{2+} chains and alternation of Ta and O rows, i.e., $(TaO)^{3+}$ units as extended defects, fill the pentagonal tunnels; slight nonstoichiometry in $Ba_{0.5-x}TaO_{3-x}$ (x = 0−0.1) leads to framework oxygen vacancies and cationic deficiency in both square and pentagonal tunnels (free of $(TaO)^{3+}$ units); phase separation into two closely related $(TaO)^{3+}$-free and $(TaO)^{3+}$-containing TTB phases occurs for the intermediate compositions.[10] The introduction of alternating M−O rows into the pentagonal tunnels via tuning the nonstoichiometry could offer an extra freedom for manipulation of composition and property of the TTB materials.[10]

Here, we report two new TTB superstructures of highly nonstoichiometric $Ba_{0.22}TaO_{2.72}$ (x = 0.28) and $Ba_{0.175}TaO_{2.675}$ (x = 0.325) materials arising from different ordering of interpolation of Ba^{2+} chains and $(TaO)^{3+}$ rows in the pentagonal tunnels. These two ordered TTB superstructures are compared with the simple TTB structures of stoichiometric $Ba_6GaTa_9O_{30}$ isolated in the $BaO-Ga_2O_3-Ta_2O_5$ system and slightly nonstoichiometric $Ba_{0.4}TaO_{2.9}$ (x = 0.1) material. The temperature dependency of cell parameters and dielectric behaviors for these materials are characterized and discussed in terms of the nonstoichiometry as well as the associated point and extended defects in the tunnels of these TTB structures.

EXPERIMENTAL SECTION

Polycrystalline samples of $Ba_{0.5-x}TaO_{3-x}$ (x = 0.1, 0.28, 0.325) and $Ba_6GaTa_9O_{30}$ were synthesized by high temperature solid state reaction using $BaCO_3$ (99.99%), Ga_2O_3 (99.99%), and Ta_2O_5 (99.99%) as starting materials, which were weighed according to the aimed stoichiometries and mixed in ethanol. The mixtures were calcined at 1473 K for 12 h and were pressed into pellets using cold-isostatic pressing under a pressure of 200 MPa. The $Ba_6GaTa_9O_{30}$ composition was fired at an optimal temperature of 1723 K for 12 h, leading to a pellet of ∼93% relative density. The $Ba_{0.4}TaO_{2.9}$ and $Ba_{0.175}TaO_{2.675}$ compositions were fired at 1873 K for 24 h, allowing the relative densities for the pellets to reach ∼98% and ∼95%, respectively, while the $Ba_{0.22}TaO_{2.72}$ composition was fired at 1873 K for 60 h, leading to a pellet with only ∼75% relative density. For structural investigation using synchrotron powder diffraction (SPD) and constant wavelength neutron powder diffraction (NPD), ∼8 g of $Ba_6GaTa_9O_{30}$, $Ba_{0.22}TaO_{2.72}$, and $Ba_{0.175}TaO_{2.675}$ powder samples were prepared by firing the calcined powders at 1473 K for 24 h with an intermediate grinding for $Ba_6GaTa_9O_{30}$ or at 1873 K for 72 h for $Ba_{0.22}TaO_{2.72}$ or 60 h for $Ba_{0.175}TaO_{2.675}$ with several intermediate grindings to ensure the phase equilibration was reached.

The phase assemblages were examined by laboratory X-ray powder diffraction (XRD) using a D8 ADVANCE powder diffractometer operating with Cu Kα radiation at 40 kV and 40 mA. Variable temperature X-ray diffraction (VTXRD) from room temperature to 1323 K was performed on a Panalytical X'Pert PRO diffractometer with Cu Kα radiation, equipped with an Anton Parr HTK 1200N high temperature attachment. The XRD data were collected over a 2θ range of 10−80° for ∼20 min at each temperature on heating and cooling. High-intensity and high-resolution SPD data were collected on the 11BM diffractometer at the Advanced Photon Source (Argonne National Laboratory, US). The sample powder was loaded in a 0.3 mm diameter glass capillary, and data were collected at room temperature over the 0.5−60° 2θ range using a step size of 0.001° and wavelength of λ = 0.413796 Å (for $Ba_{0.175}TaO_{2.675}$ and $Ba_{0.22}TaO_{2.72}$) and 0.413957 Å (for $Ba_6GaTa_9O_{30}$). The sample was spun at 60 Hz to improve powder averaging of the crystallites. NPD data (λ = 1.225 Å) were collected at room temperature on the 3T2 diffractometer (Laboratoire Léon Brillouin, France) over the 2θ range of 4.5−121° with a 0.05° step size for 22 h. The Rietveld analysis[11] was carried out using the Topas Academic.[12] Bond valence sums (BVSs) were calculated by Brown and Altermatt's method.[13] Electron diffraction (ED) experiments were performed on a Philips CM20 transmission electron microscope (TEM) fitted out with an Oxford EDS analyzer. The sample was first crushed in ethanol, and a drop of the solution with the small crystallites in suspension was deposited onto a carbon-coated copper grid.

Ac impedance spectroscopy (IS) measurement in air was performed from room temperature to 1173 K using a Solartron 1260A impedance/gain-phase analyzer over the frequency range from 10^{-1} to 10^7 Hz. Prior to the IS measurement, the pellet was coated with gold paste on opposite faces and fired at 773 K for 30 min to burn out the organic components to form electrodes. The measured capacitance from the impedance data was corrected for calculating the permittivity of the material itself by subtracting the blank contribution arising from the sample holder and connection cables, which was measured on an open circuit without the pellet. The complex permittivity from room temperature up to 70 K of the pellets coated with silver paste was measured under a nitrogen atmosphere, using a Tonghui TH2828A LCR meter in a Mercury iTC cryogenic environment controller of Oxford Instrument. Electromotive force measurements were performed using an oxygen concentration cell of N_2/sample/air to assess the oxide ion conduction in the dense triple TTB $Ba_{0.175}TaO_{2.675}$ sample in 600−800 °C. The partial oxygen pressure in the N_2 gas was determined by an YSZ sensor at 600 °C, which was used to calculate the theoretical voltage of the N_2/sample/air cell according to the Nernst equation. The oxygen transport numbers were then calculated using the ratio of experimental to calculated voltages.

RESULTS

TTB Superstructure Phases in $Ba_{0.5-x}TaO_{3-x}$. As demonstrated during our previous work, the $Ba_{0.5-x}TaO_{3-x}$ (x = 0.25−0.325) solid solution formed a simple TTB crystalline phase with disordered interpolation of Ba^{2+} and $(TaO)^{3+}$ groups into pentagonal tunnels in the TTB structure when it was heated at 1473 K. Once the firing temperature was increased above 1773 K, complex TTB superstructures dependent on the compositions were observed on these highly nonstoichiometric $Ba_{0.5-x}TaO_{3-x}$ compositions. Figure 1 compares the room-temperature SPD data of superstructure TTB phases, $Ba_{0.22}TaO_{2.72}$ and $Ba_{0.175}TaO_{2.675}$ fired at 1873 K, with simple TTB phases, the stoichiometric $Ba_6GaTa_9O_{30}$ and nonstoichiometric $Ba_{0.22}TaO_{2.72}$ (fired at 1473 K) compositions. Two sets of extra reflections are clearly visible (Figure 1a), with the largest d-spacing (Å) values ∼17.7 and ∼18.7 for $Ba_{0.22}TaO_{2.72}$ and $Ba_{0.175}TaO_{2.675}$, respectively. This indicates formation of two different TTB superstructures.

An autoindexing analysis of the room-temperature SPD pattern of the $Ba_{0.175}TaO_{2.675}$ (x = 0.325) composition fired at 1873 K was performed. Both Dicvol[14] and Treor[15] indexing routines led to the same orthorhombic solution, a ∼ 12.53 Å, b ∼ 37.49 Å, and c ∼ 3.912 Å, with good reliability factors. This result implies a triple TTB superstructure formation via tripling the b-axis of the simple TTB unit cell (i.e., $a_O \sim a_T$, $b_O \sim 3b_T$, $c_O \sim c_T$ where O and T denote orthorhombic and tetragonal, respectively), which is consistent with the results reported by Vanderah et al.[16] A subsequent Inorganic Crystal Structure Database (ICSD) search using similar cell parameters showed five orthorhombic compounds corresponding to the triple TTB structures: $Nb_{13.5}W_{20.5}O_{95.25}$ (*Pbam*, ICSD #24113),[17] $Na_{13}Nb_{35}O_{94}$ (*Pba*2, ICSD #24882),[18] $Nb_{22}W_{20}O_{102}$ (*Pbam*, ICSD #29254),[19] $Nb_{18}W_{16}O_{93}$ (*Pbam*, ICSD #29255),[19] and $Nb_{6.7}W_{10.3}O_{47}$ ($P2_12_12$, ICSD #90928).[20] In order to confirm the cell parameters and to find out the possible space groups of our material, we then performed an electron diffraction (ED) study on numerous crystallites. The reconstruction of the

DOI: 10.1021/acs.inorgchem.5b01098
Inorg. Chem. 2015, 54, 8978−8986

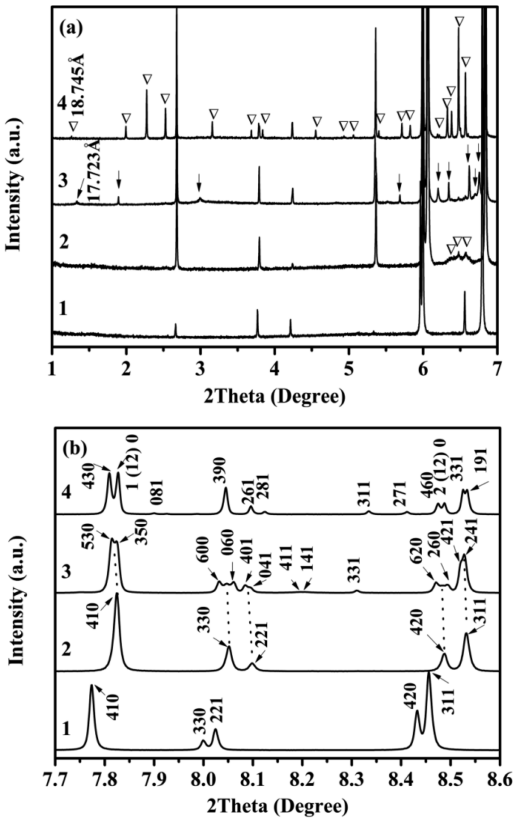

Figure 1. Comparison of SPD data of $Ba_6GaTa_9O_{30}$ (simple TTB, pattern 1), $Ba_{0.22}TaO_{2.72}$ (simple TTB, pattern 2), $Ba_{0.22}TaO_{2.72}$ ($\sqrt{2}$-type TTB, pattern 3), and $Ba_{0.175}TaO_{2.675}$ (triple TTB, pattern 4). (a) Enlargement of the low-angle plots in the 1−7° 2θ region for each pattern showing extra reflections from the superstructure formations: the reflections marked by the arrows and the up-side-down triangles denotes formation of the $\sqrt{2}$-type and triple TTB superstructures, respectively. (b) *hkl* indices of each phase in the 7.7−8.6° 2θ range: tetragonal cells for patterns 1 ($a \sim 12.59$ Å, $c \sim 3.959$ Å) and 2 ($a \sim 12.51$ Å, $c \sim 3.914$ Å); orthorhombic cells for patterns 3 ($a \sim 17.72$ Å, $b \sim 17.67$ Å, $c \sim 3.917$ Å) and 4 ($a \sim 12.53$ Å, $b \sim 37.49$ Å, $c \sim 3.912$ Å). The dash lines mark the reflections of the simple TTB phase in the mixed-phase $Ba_{0.22}TaO_{2.72}$ composition.

reciprocal space obtained by tilting around the crystallographic axes confirmed the orthorhombic cell determined above. A characteristic [001] electron diffraction pattern for this triple TTB phase is presented in Figure 2a. The sharp spots and the absence of any diffuse streaks both demonstrate the good crystallization of the sample and rule out the existence of any stacking defects. No condition limiting the general *hkl* reflections was observed during the reciprocal lattice reconstruction, leading to the assignment of a primitive lattice. The only extra conditions, *h*00: $h = 2n$ and 0*k*0: $k = 2n$, unambiguously implied the choice of the nonpolar $P2_12_12$ space group, similar to the $Nb_{6.7}W_{10.3}O_{47}$ compound.[20]

The reflections of the superstructure TTB phase in the $Ba_{0.22}TaO_{2.72}$ composition (fired at 1873 K) can be indexed using a different unit cell, $a \sim 17.720$ Å, $b \sim 17.667$ Å, and $c \sim 3.916$ Å, which was confirmed by the ED study (Figure 2b). This result indicated a $\sqrt{2}$-type TTB superstructure for the $Ba_{0.22}TaO_{2.72}$ composition. Careful examination of SPD data of $Ba_{0.22}TaO_{2.72}$ revealed its mixed phase nature (Figure 1b); i.e., the sample contains a simple TTB phase in addition to the $\sqrt{2}$-type TTB phase. The phase formations of other $Ba_{0.5-x}TaO_{3-x}$

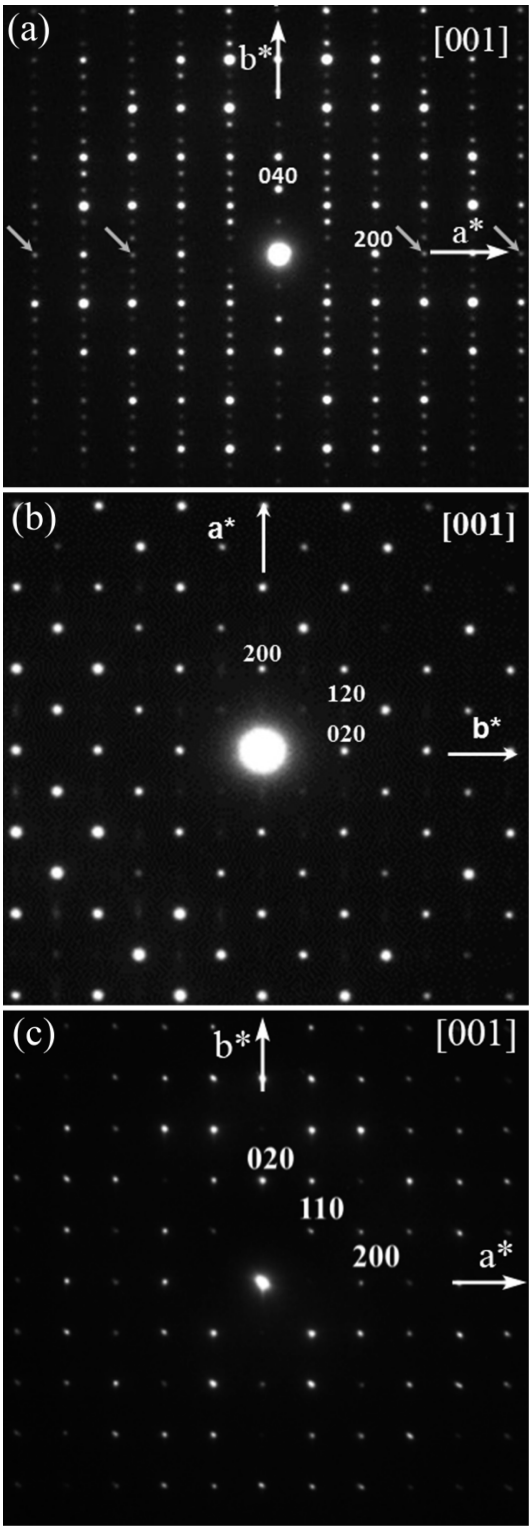

Figure 2. Electron diffraction patterns of (a) triple TTB $Ba_{0.175}TaO_{2.675}$, (b) $\sqrt{2}$-type TTB $Ba_{0.22}TaO_{2.72}$, and (c) simple TTB $Ba_6GaTa_9O_{30}$ compositions recorded along the [001] direction. White arrows point to forbidden reflections appearing from double diffraction. The indexations for (a) $Ba_{0.175}TaO_{2.675}$, (b) $Ba_{0.22}TaO_{2.72}$, and (c) $Ba_6GaTa_9O_{30}$ were performed using the triple (orthorhombic, $a \sim 12.53$ Å, $b \sim 37.49$ Å, $c \sim 3.912$ Å), $\sqrt{2}$-type (orthorhombic, $a \sim 17.72$ Å, $b \sim 17.67$ Å, $c \sim 3.917$ Å), and simple TTB (tetragonal, $a \sim 12.59$ Å, $c \sim 3.959$ Å) cells, respectively.

DOI: 10.1021/acs.inorgchem.5b01098
Inorg. Chem. 2015, 54, 8978−8986

compositions (x = 0.25, 0.30) were also examined at 1873 K. Similarly to the $Ba_{0.22}TaO_{2.72}$ (x = 0.28) case, the x = 0.25 composition ($Ba_{0.25}TaO_{2.75}$) was also found to contain a mixture of simple TTB and $\sqrt{2}$-type TTB superstructure phases, while in the x = 0.30 composition ($Ba_{0.2}TaO_{2.7}$), apart from the simple and $\sqrt{2}$-type TTB phases, a minor triple TTB superstructure phase was also observed. Prolonged annealing at 1873 K or firing at higher temperatures up to 2023 K or lower temperatures within 1773−1823 K provides no significant change to the phase formation in these compositions, so that it was not possible to obtain a single-phase $\sqrt{2}$-type TTB superstructure material.

Triple TTB Superstructure. The precise structure determination of the triple-TTB phase $Ba_{0.175}TaO_{2.675}$ was performed using a combination of Rietveld refinements performed on both synchrotron and neutron powder diffraction data. The starting model was based on the $Nb_{6.7}W_{10.3}O_{47}$ structure[20] using the orthorhombic cell parameters previously determined by ED and autoindexing. In a first step, SPD data were used to refine the cell parameters and the cationic positions. In a second step, the NPD pattern was used for refinement of the oxygen positions. Considering the high statistics and high resolution of the data, very good reliability factors were obtained (SPD: R_p = 8.46%, R_{wp} = 10.96%; NPD: R_p = 1.73%, R_{wp} = 2.14%). The fits of both the SPD and NPD are presented in Figure 3. The final atomic coordinates and Ba−O and Ta−O interatomic distances are gathered in Tables S1 and S2. The structure contains 2 Ba, 12 Ta, and 24 O crystallographic sites. All these positions are located on 4*c* positions, apart from Ta2 and O2 which occupy 2*b* sites (Table S1). The tripling of the TTB structure originates from the filling order in the pentagonal tunnels. The 3 different pentagonal tunnels (labeled as P1, P2, and P3 in Figure 4a) are filled by Ta9(O23), Ba1, and Ba2. The site occupancy refinement over these three pentagonal tunnels showed that the P1 tunnel appears to be fully occupied by Ta9 and O23, whereas Ba1 and Ba2 sites in P2 and P3 tunnels show partial occupancies of 80(3)% and 77(3)%, respectively. In other words, the $(TaO)^{3+}$ filling in the pentagonal tunnels is completely ordered on the P1 tunnels along the *b*-axis. The square tunnels in this triple TTB structure remain empty (labeled as S1 and S2 in Figure 4a). Regarding the triangular tunnels, difference Fourier map inspection revealed the presence of Ta crystallographic sites within all of the 3 different triangular tunnels (namely, Ta10, Ta11, and Ta12 showing, respectively, 10(2)%, 6(2)%, and 10(2)% occupancies in Table S1). Although the content of Ta within these triangular tunnels appears rather small, its presence clearly benefits the refinements, especially small peak intensities clearly observed on the SPD data. It is remarkable to note that the final refined overall composition $Ba_{6.3(2)}Ta_{35.1(1)}O_{94}$, obtained from both SPD and NPD data Rietveld refinements, respects global electroneutrality (considering Ba^{2+} and Ta^{5+}cations) and matches the nominal composition, although no specific constraints were used. The atomic displacement factors (ADPs) for all the crystallographic sites for the triple TTB phase except for the Ta10−Ta12 sites were refined freely without any constrains during the refinement. Two negative ADP values were obtained for the Ba1 and O4 sites only. Although they are nonphysically meaningful, their near-zero values (the negative value is within the estimated standard deviation) show validity for both sites. The refined ADPs of Ta and O sites are slightly scattered (Table S1). However, there is no unusually large ADPs for Ta and O sites (except for O2 which has a slightly large ADP ∼ 0.034(5) Å^2). Given the complexity of the triple TTB superstructure, the refined structural parameters for the triple TTB phase are acceptable. The triple TTB superstructure described here in the noncentrosymmetric $P2_12_12$ space group is close to the centrosymmetric supergroup *Pbam* model as *z* values for all the crystallographic sites are close to 0/1 or 0.5 (Table S1).

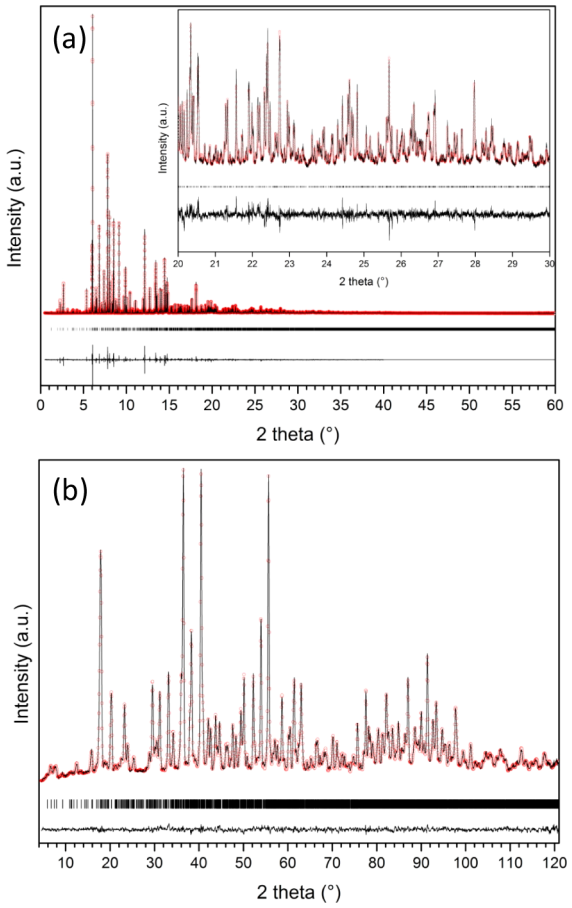

Figure 3. Rietveld fits of (a) SPD and (b) NPD data of triple-TTB $Ba_{0.175}TaO_{2.675}$. Red dots represent the observed data; black lines, the calculated ones; Bragg ticks, the peak positions; the black curve underneath shows the difference between the observed and calculated patterns. The inset on the refined synchrotron diffractogram corresponds to the 20−30° (2θ) region enlargement.

$\sqrt{2}$-type TTB Superstructure. The structure solution of the orthorhombic $\sqrt{2}$-type TTB superstructure was carried out using SPD, NPD, and ED data of $Ba_{0.22}TaO_{2.72}$ composition, in which the superstructure formation is not homogeneous, displaying mixed phase nature, as described above. The lengths for the *a* and *b* axes are very close (the difference is less than 0.1 Å) in the orthorhombic $\sqrt{2}$-type TTB structure. This makes the assignment of the reciprocal *a** and *b** axes on ED patterns difficult, given the lack of accuracy on the *d*-spacing values using electron diffraction compared with X-ray diffraction. A combined use of electron diffraction with X-ray powder diffraction data has to be considered to unambiguously determine the space group. The relationship between the orthorhombic $\sqrt{2}$-type TTB superstructure and the simple TTB unit cells can be described as $a_O \sim a_T - b_T$, $b_O \sim a_T + b_T$, $c_O \sim c_T$. Such unit-cell transformation leads to several possible candidate orthorhombic space groups for the $\sqrt{2}$-type TTB

DOI: 10.1021/acs.inorgchem.5b01098
Inorg. Chem. 2015, 54, 8978−8986

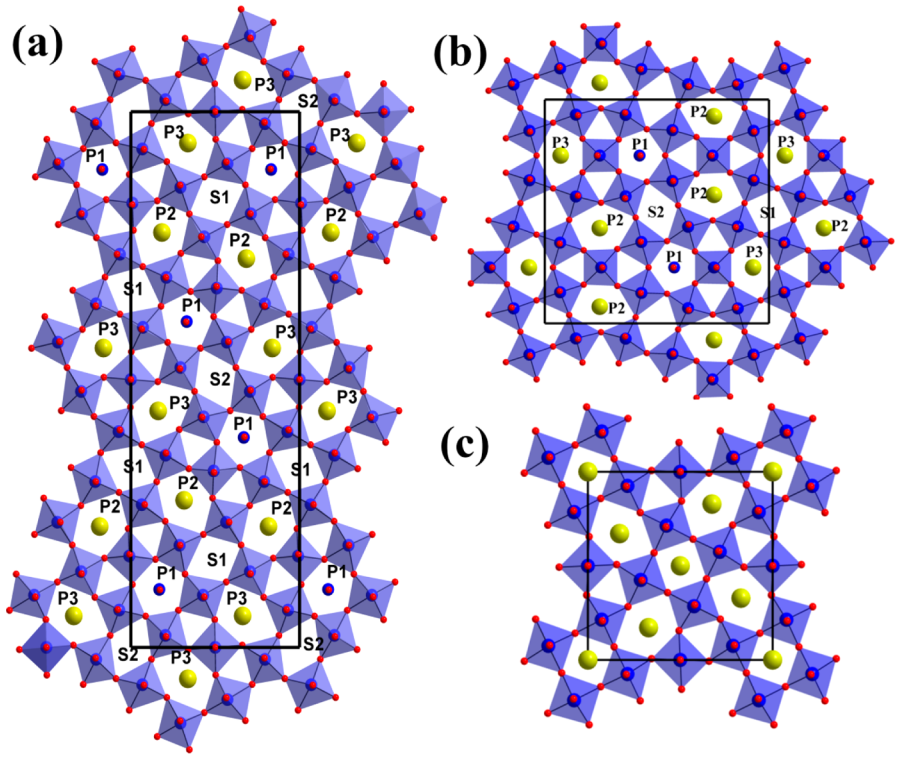

Figure 4. Comparison of [001] projections of crystal structures for triple-TTB $Ba_{0.175}TaO_{2.675}$ (a), $\sqrt{2}$-type TTB $Ba_{0.22}TaO_{2.72}$ (b), and simple TTB $Ba_6GaTa_9O_{30}$ (c). In (a) and (b), P1, P2, and P3 denote three crystallographically distinct pentagonal tunnels, and only one species of either $(TaO)^{3+}$ (P1) or Ba^{2+} (P2 and P3) is shown in these pentagonal tunnels. S1 and S2 denote two crystallographically distinct empty square tunnels.

superstructure: C*mmm* (No. 65) and its subgroups, P*mmn* (No. 59), P*bam* (No. 55), P*bmn* or P*man* (No. 53), P*mam* or P*bmm* (No. 51), P*ban* (No. 50), and P*mmm* (No. 47) with primitive lattice, derived from the tetragonal supergroup P4/*mbm* of the simple TTB structure. Each candidate space group was examined against ED data, followed by Pawley fits performed on SPD data. No reflection condition for the general *hkl* reflections was observed on the SPD and ED data, which suggested primitive lattice and excluded the C*mmm* space group easily. The subsequent Pawley fits on the SPD data using the subgroups of C*mmm* suggested two possible space groups P*bmm* (No. 51) and P*mmm* (No. 47) for the $\sqrt{2}$-type TTB superstructure. The distinction of 0*k*0 ($k = 2n + 1$) reflections observed in the ED pattern (Figure 2b) agrees well with the P*bmm* symmetry. Therefore, the $\sqrt{2}$-type TTB superstructure was refined using the P*bmm* space group based on both SPD and NPD data of $Ba_{0.22}TaO_{2.72}$ composition with the simple TTB phase included in the refinement, where the occupancies of Ba, Ta, and O in pentagonal tunnels were refined without compositional constraints except for the occupancies of Ta and O atoms which were fixed to be identical in the same pentagonal tunnels. Rietveld fits of SPD and NPD data of mixed-phase $Ba_{0.22}TaO_{2.72}$ sample are shown in Figure S1. The final refined structural parameters and the bond lengths for the $\sqrt{2}$-type TTB superstructure are given in Tables S3 and S4.

Figure 4b shows a schematic plot of the $\sqrt{2}$-type TTB structure of $Ba_{0.22}TaO_{2.72}$. In the $\sqrt{2}$-type TTB structure of $Ba_{0.22}TaO_{2.72}$, the square tunnels also remain empty and the distribution of Ba^{2+} and $(TaO)^{3+}$ species among the three crystallographically distinct pentagonal tunnels (labeled as P1, P2, and P3, corresponding to the Ba1 (Ta7−O18), Ba2 (Ta8−O19), and Ba3 (Ta9−O20) sites in Table S3, respectively) displays partial ordering with preference of the alternate $(TaO)^{3+}$ rows on P1 over the other two pentagonal tunnels (P2 and P3). Similarly to the triple TTB structure, a small amount of Ta atoms occupancies (∼6−9%) was also revealed in the triangular tunnels (sites Ta10, Ta11, Ta12 in Table S3). The refined composition $Ba_{5.10(1)}Ta_{22.72(1)}O_{62.12(1)}$ for the $\sqrt{2}$-type TTB phase agrees well with the nominal composition. The existence of the minor simple TTB phase in the mixed-phase $Ba_{0.22}TaO_{2.72}$ sample was confirmed by a two-phase Rietveld refinement, which gave mass percentages of ∼79 and ∼21 wt % for the $\sqrt{2}$-type TTB and simple TTB phases, respectively, and showed that the minor simple TTB phase also contained $(TaO)^{3+}$ species in the pentagonal tunnel with a refined composition $Ba_{2.29(2)}Ta_{11.26}O_{31.26(1)}$, close to $Ba_{0.22}TaO_{2.72}$. This suggests that the coexistence of $\sqrt{2}$-type and simple TTB phases in the $Ba_{0.22}TaO_{2.72}$ sample is due to inhomogeneous ordering of Ba^{2+} and $(TaO)^{3+}$ species in the pentagonal tunnels through the sample, instead of the phase separation into different compositions. The ED experiments showed that both phases coexist but in different crystallites and no domain feature with different symmetries (for example, presence of diffuse streaks) was observed in the same crystals in the mixed-phase $Ba_{0.22}TaO_{2.72}$ sample.

Simple TTB Structures. The simple TTB structures of both stoichiometric $Ba_6GaTa_9O_{30}$ and slightly nonstoichiomtric $Ba_{0.4}TaO_{2.9}$ were studied for comparison with the triple and $\sqrt{2}$-type TTB superstructures. The ED patterns (Figures 1c and S2) collected on these two compositions confirmed the tetragonal cell. The reflection conditions are consistent with the P4/*mbm* space group. A combined SPD and NPD refinement was carried out for the $Ba_6GaTa_9O_{30}$ compound, which showed that Ga atoms are distributed over the two octahedral sites (Ta1/Ga1 (2*c*) and Ta2/Ga2 (8*j*) in Table S5) in a disordered manner. Reducing the symmetry of the space group to the

DOI: 10.1021/acs.inorgchem.5b01098
Inorg. Chem. 2015, 54, 8978−8986

polar P4*bm* did not significantly improve the fit, and the temperature dependency of dielectric permittivity (described below) did not show ferroelectric or relaxor-like transition within 100−800 K, so that the polar P4*bm* space group could be ruled out for $Ba_6GaTa_9O_{30}$ at ambient temperature. The Rietveld plots of the SPD and NPD data of $Ba_6GaTa_9O_{30}$ are shown in Figure S3. The final refined structural parameters and the bond lengths for $Ba_6GaTa_9O_{30}$ are listed in Tables S5 and S6, respectively. The Rietveld analysis of $Ba_{0.4}TaO_{2.9}$ structure was performed using the laboratory XRD data only. The occupancies on the Ba and oxygen sites were refined subject to the charge neutrality constraint, and the oxygen vacancies were presumed to be disordered due to the insensitivity of XRD to the light O atoms. This led to a $Ba_{4.29(1)}Ta_{10}O_{28.99(8)}$ refined composition, which is closed to the nominal one. The refinement shows that the square tunnels are not completely empty but contain ∼18% Ba cations, and the pentagonal tunnels contain ∼2% Ba vacancies. Figure S4 shows the Rietveld plot of the XRD data for $Ba_{0.4}TaO_{2.9}$. Tables S7 and S8 list the final refined structural parameters and bond lengths for $Ba_{0.4}TaO_{2.9}$, respectively.

Thermal Expansion. Variable temperature X-ray diffraction data were collected on simple TTB phases ($Ba_6GaTa_9O_{30}$, $Ba_{0.4}TaO_{2.9}$, and $Ba_{0.22}TaO_{2.72}$) and TTB superstructure phases ($Ba_{0.175}TaO_{2.675}$ and $Ba_{0.22}TaO_{2.72}$) from ambient temperature up to 1323 K. The high temperature XRD patterns of all of these samples appear similar to those at ambient temperature except for the peak position shift due to the thermal expansions of the samples and sample holder. No apparent evidence for phase transitions can be discerned from laboratory VTXRD data. The refined cell parameters (Figure 5) from these VTXRD data upon heating show that the cell expansion of the stoichiometric $Ba_6GaTa_9O_{30}$ is linear over the measured temperature region; on the contrary, the nonstiochiometric $Ba_{0.4}TaO_{2.9}$, $Ba_{0.22}TaO_{2.72}$ (both simple and $\sqrt{2}$-type TTB phases), and $Ba_{0.175}TaO_{2.675}$ (triple TTB phase) displayed apparent curvature on the *c*-axis expansion around 600 K. Such thermal expansion behavior is reproducible on cooling. The curvature on the thermal expansion of the *c*-axis was also observed on the $\sqrt{2}$-type TTB phase in mixed-phase $Ba_{0.25}TaO_{2.75}$ composition (Figure S5).

Electrical Properties. Impedance spectroscopy measurements were performed to obtain the dielectric permittivity and electrical conductivity for the TTB oxides $Ba_{0.5-x}TaO_{3-x}$. At room temperature, the dense pellets of $Ba_6GaTa_9O_{30}$, $Ba_{0.4}TaO_{2.9}$, and $Ba_{0.175}TaO_{2.675}$ possess high dielectric permittivity values of ∼80, 95, and 60 at 1 MHz, respectively. Figure 6 shows the temperature dependencies of permittivity, ε_r', of dense $Ba_6GaTa_9O_{30}$, $Ba_{0.4}TaO_{2.9}$, and $Ba_{0.175}TaO_{2.675}$ pellets. The $Ba_6GaTa_9O_{30}$ pellet showed frequency independent permittivity (10^3−10^6 Hz), which decreased monotonically with the temperature. On the contrary, the permittivity values for $Ba_{0.4}TaO_{2.9}$ and $Ba_{0.175}TaO_{2.625}$ pellets were frequency dependent and displayed rather broad, frequency-dependent relaxation peaks above room temperature within 10^3−10^5 Hz, while the dielectric relaxation peaks at the higher frequency of 1 MHz were hardly noticeable. Complex impedance plot analysis (Figure S6) revealed both $Ba_{0.175}TaO_{2.675}$ and $Ba_{0.22}TaO_{2.72}$ pellets of TTB superstructures possess ionic conduction with higher bulk conductivities than those for simple TTB $Ba_6GaTa_9O_{30}$ and $Ba_{0.4}TaO_{2.9}$ materials. The mixed $\sqrt{2}$-type and simple TTB phase $Ba_{0.22}TaO_{2.72}$ sample displayed essentially identical conductivity with that for the disordered

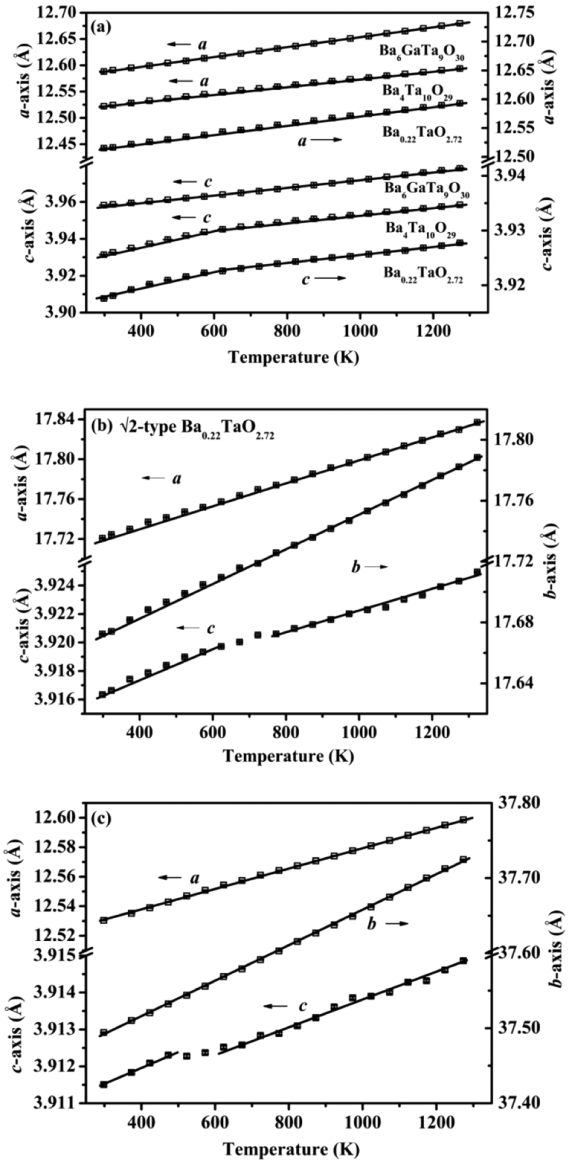

Figure 5. Temperature dependencies of the cell parameters of $Ba_6GaTa_9O_{30}$, $Ba_{0.4}TaO_{2.9}$, and $Ba_{0.22}TaO_{2.72}$ (disordered) (a), $Ba_{0.22}TaO_{2.72}$ ($\sqrt{2}$-type TTB) (b), and $Ba_{0.175}TaO_{2.675}$ (triple TTB) (c) from ambient temperature to 1323 K.

phase (Figure S6d), while the $Ba_{0.175}TaO_{2.675}$ pellet displayed slightly lower bulk conductivity (10^{-8}−10^{-4} S/cm in the 250−800 °C region) than the $Ba_{0.22}TaO_{2.72}$ sample (Figure S6d). The details on impedance data analysis for obtaining the bulk conductivities and assessing ionic conduction in the materials are provided in the Supporting Information.

Our previous investigation has identified ionic conduction for the disordered $(TaO)^{3+}$-containing TTB $Ba_{0.22}TaO_{2.72}$ composition, and the impedance measurements under the O_2 and N_2 atmosphere ruled out the oxide ion conduction through the oxygen-partial-pressure independent electrode response. Thus, the ionic conduction was attributed to the divalent Ba^{2+} conduction.[10] The EMF measurements in this study gave near-zero oxygen transport numbers (∼0.03) in 600−800 °C for triple TTB superstructure phase $Ba_{0.175}TaO_{2.675}$, further confirming the limited oxide ion conduction in these highly nonstiochiometric TTB oxides.

DOI: 10.1021/acs.inorgchem.5b01098
Inorg. Chem. 2015, 54, 8978−8986

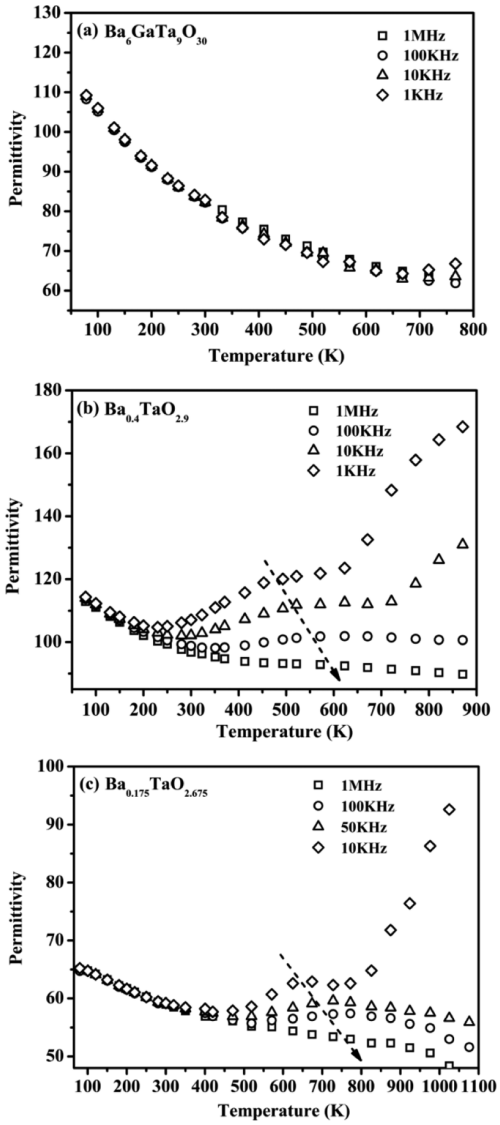

Figure 6. Temperature dependency of dielectric permittivity, ε_r', at different frequencies for $Ba_6GaTa_9O_{30}$ (a), $Ba_{0.4}TaO_{2.9}$ (b), and $Ba_{0.175}TaO_{2.675}$ (c) pellets. The arrows indicate increasing frequency.

DISCUSSION

Our previous investigation has revealed that the stability of the nonstoichiometric TTB $Ba_{0.5-x}TaO_{3-x}$ compositions is associated with emptying the tunnels, filling $(TaO)^{3+}$ rows into the pentagonal tunnels, and balancing the octahedral framework oxygen vacancies.[10] In the slightly nonstoichiometric $(TaO)^{3+}$-free $Ba_{0.4}TaO_{2.9}$, the square and pentagonal tunnels are partially filled by Ba^{2+} cations and the framework oxygen sites contain a small amount of oxygen vacancies (~3%) due to the cationic deficiency in the tunnels. With the composition drifting to the Ta_2O_5-rich side in $Ba_{0.5-x}TaO_{3-x}$, it is expected that the TTB structure is not tolerant of high-level emptiness of the tunnels and framework oxygen vacancies. Thus, the $(TaO)^{3+}$ groups from Ta_2O_5 in highly nonstoichiometric $Ba_{0.5-x}TaO_{3-x}$ composition fill the pentagonal tunnels, and the remaining oxygen atoms from the Ta_2O_5 excess enter into the framework of oxygen sites; both processes reduce the tunnel emptiness and framework oxygen vacancies, thus stabilizing the highly nonstoichiometric $(TaO)^{3+}$-containing phases. The filling of $(TaO)^{3+}$ groups into pentagonal tunnels leads to a 7-coordinate pentagonal bipyramidal environment for the Ta atoms in the pentagonal tunnels.[10]

The interpolation of Ba^{2+} and $(TaO)^{3+}$ groups into pentagonal tunnels in the highly nonstoichiometric $(TaO)^{3+}$-containing $Ba_{0.5-x}TaO_{3-x}$ went through a disorder−order transition at high temperature above 1773 K. This means that the cationic ordering in the highly nonstoichiometric $Ba_{0.5-x}TaO_{3-x}$ is a thermally activated process, similar to the B-cationic ordering in the well-known complex perovskites.[21−23] The filling-order in the pentagonal tunnels in $Ba_{0.5-x}TaO_{3-x}$ demonstrates strong dependency on the stoichiometry: in $Ba_{0.22}TaO_{2.72}$ (x = 0.28), the interpolation of Ba^{2+} and $(TaO)^{3+}$ groups is partially ordered along the *ab*-plane of the simple TTB structure, forming the $\sqrt{2}$-type TTB superstructure, while in $Ba_{0.175}TaO_{2.675}$ (x = 0.325) with higher Ta/Ba ratio, the pentagonal tunnel filling is completely ordered along the *b*-axis of the simple TTB structure, forming a triple ordered TTB superstructure with one-third of the pentagonal tunnels filled by $(TaO)^{3+}$ rows and the remaining pentagonal tunnels filled by the incomplete Ba^{2+} cationic chains. The filling of $(TaO)^{3+}$ row into the pentagonal tunnel leads to size contraction of the pentagonal tunnel in comparison with the normal pentagonal tunnels occupied by the Ba^{2+}cations, as well as the distortion of the framework octahedra.[10] This could in consequence make the five nearest pentagonal tunnels neighboring the $(TaO)^{3+}$-containing pentagonal tunnel unfavorable for accommodating the $(TaO)^{3+}$ rows.[10] This is well evidenced by the triple ordered TTB structure of $Ba_{0.175}TaO_{2.675}$ (in Figure 4a), where the five pentagonal tunnels (two P2 and three P3) neighboring the $(TaO)^{3+}$-occupied P1 tunnels are occupied by Ba^{2+}.

According to the refinement results, the formulas for the triple TTB $Ba_{0.175}TaO_{2.675}$ and $\sqrt{2}$-type TTB $Ba_{0.22}TaO_{2.72}$ may be described, respectively, as $(Ba)_{2.1}(TaO)_{1.33}[Ba]_0\{Ta\}_{0.35}Ta_{10}O_{30}$ and $(Ba)_{2.55}(TaO)_{1.06}[Ba]_0\{Ta\}_{0.3}Ta_{10}O_{30}$, where (), [], and {} denote the pentagonal, square, and triangle tunnel sites. This means that the triple TTB phase contains more $(TaO)^{3+}$ rows and less Ba^{2+} in the pentagonal tunnels than those in the $\sqrt{2}$-type TTB phase and the choice of triple and $\sqrt{2}$-type ordering in $Ba_{0.5-x}TaO_{3-x}$ relies on the content of $(TaO)^{3+}$ rows in the pentagonal tunnels. It is also remarkable that the smallest triangular tunnels in these two TTB superstructures contain a small amount of Ta^{5+} cations. Filling Ta^{5+} cations into the triangular tunnels further eliminates the framework oxygen vacancies with respect to charge neutrality, giving the refined compositions for these two TTB superstructure phases good consistency with nominal compositions. The calculated BVSs for these Ta^{5+} cations in the triangle tunnels suggest under-bonding environments. The content of Ta within these triangular tunnels appears rather small, i.e., about or below 10%, which does not allow highly accurate distances between these extra Ta sites and the framework oxygen atoms to be obtained in these average structures. Locally, the framework octahedra defining the triangle tunnels containing the Ta^{5+} cations are expected to be distorted for shortening/elongating the distances of Ta^{5+} with the framework oxygen atoms to provide a more reasonable bonding environment for these Ta^{5+} cations in the triangle tunnels.

In $Ba_{0.5-x}TaO_{3-x}$ TTB materials, the tunnel filling and emptying also demonstrate the impact on their electrical conductivity behavior. In the $(TaO)^{3+}$-containing phase, the completely empty square tunnels that are expanded by the filling $(TaO)^{3+}$ rows into the neighboring pentagonal tunnels

DOI: 10.1021/acs.inorgchem.5b01098
Inorg. Chem. 2015, 54, 8978−8986

favor the intertunnel hopping of Ba^{2+} cations between the pentagonal and square tunnels and facilitate the motion of large and heavy Ba^{2+} cations in the square tunnels.[10] The $(TaO)^{3+}$-free $Ba_{0.4}TaO_{2.9}$ contains ~18% Ba^{2+} cations in the square tunnels and thus does not meet the critical condition for Ba^{2+} motion of empty square tunnels, which accounts for its lower conductivity. The essentially identical conductivities for the ordered and disordered $Ba_{0.22}TaO_{2.72}$ (Figure S6d) suggest that the ordering of interpolating Ba^{2+} and $(TaO)^{3+}$ groups into pentagonal tunnels has little influence on the conductivity. This is consistent with the key role on the Ba^{2+} motion of the empty square tunnels, which are not affected by the filling ordering in the pentagonal tunnels. Compared with $Ba_{0.22}TaO_{2.72}$, the less Warburg-type electrode response (Figure S6a) and lower conductivity of the triple $Ba_{0.175}TaO_{2.675}$ pellet (Figure S6d) is consistent with the smaller content of Ba^{2+} cations.

It is common that the stoichiometric TTB materials (including the tetragonal parents and the lower symmetric phases) display ferroelectric or relaxor-ferroelectric behaviors. The stoichiometric tetragonal $Ba_6GaTa_9O_{30}$ material here displayed normal temperature dependency of dielectric permittivity (i.e., monotonic decrease with the temperature) within the measured temperature region from 100 to 800 K. This behavior is consistent with the nonpolar space group P4/*mbm* for $Ba_6GaTa_9O_{30}$ at room temperature and similar to that observed on the Nb-analogue $Ba_6GaNb_9O_{30}$, which showed a relaxor-ferroelectric transition just below 100 K.[4] While the slightly nonstoichiometric simple-TTB $Ba_{0.4}TaO_{2.9}$ displayed a diffuse-type dielectric relaxation above room temperature, such dielectric relaxation was also observed in the highly nonstoichiometric TTB superstructure phases with orthorhombic symmetries (Figure 6). These above-room-temperature dielectric relaxations are irrespective with the compositions, structures/symmetries, and pentagonal-filling order, which coincide with the common curvature of the *c*-axis expansion behaviors observed for all of the nonstoichiometric compositions (Figure 5) within the similar temperature regions. On the contrary, the stoichiometric $Ba_6GaTa_9O_{30}$ showing no such dielectric relaxation above the room temperature displayed linear expansion of the *c*-axis. The similar behaviors of dielectric relaxation and thermal expansion of the *c*-axis between all of the nonstoichiometric TTB compositions $Ba_{0.5-x}TaO_{3-x}$ indicate that these dielectric relaxations could have the same origin. The nonpolar symmetry for the triple TTB superstructure at room temperature may rule out the possibility of relaxor-ferroelectric transition for these above-room-temperature dielectric relaxations. Therefore, the ferroelectric or relaxor-ferroelectric transition is expected to take place at lower temperature out of the measured temperature region for the simple TTB $Ba_{0.4}TaO_{2.9}$. These dielectric relaxations are less noticeable at high frequency, 1 MHz, which suggests that the dielectric relaxations are likely to be associated with an extrinsic polarization instead of the macroscopic structural transitions, consistent with the laboratory VTXRD data that did not show apparent evidence of phase transitions over the abnormal dielectric-relaxation temperature region.

The origins of the intrinsic polarizations in the TTB materials have been classified as two kinds: one is from the off-center displacements of octahedral B cations along the *c*-axis;[4] the other one is from the octahedral tilting in the *ab*-plane.[24] The coupling of these two polarizations was used to interpret the additional dielectric relaxations in orthorhombic $Ba_2NdTi_2Nb_3O_{15}$ below the ferroelectric transition temperature.[5] Extra diffuse dielectric relaxations above the ferroelectric transition temperature have been frequently observed in ferroelectric perovskite oxides (e.g., $BaTiO_3$ and $SrTiO_3$) in the temperature region of 400−700 °C.[25] Such dielectric anomaly was linked with the short-range thermal hopping of oxygen vacancy defects, similar to the reorientation of the dipole.[25,26] In case of the nonstoichiometric TTB $Ba_{0.5-x}TaO_{3-x}$ here, these above-room-temperature dielectric relaxations could be correlated with the common structural feature of the square-tunnel emptiness, which assists the Ba^{2+} motion in the materials as revealed by the conductivity data. In other words, the local hopping of Ba^{2+} cations in the tunnels along the *c*-axis might be responsible for these abnormal dielectric relaxations. The different thermal expansion coefficients of the *c*-axis parallel to the tunnels in the different temperature regions for these nonstoichiometric $Ba_{0.5-x}TaO_{3-x}$ compositions could also be associated with tunnel filling and emptying. The coinciding dielectric relaxations and curvatures on the thermal expansion of the *c*-axis observed in the similar temperature region reveal existence of complex mechanisms associated with the tunnel filling and emptying in the nonstoichiometric TTB materials, which could stimulate further investigations.

CONCLUSION

Two complex ordered patterns of the interpolation of Ba^{2+} cationic chains and $(TaO)^{3+}$ rows in the pentagonal tunnels along the crystallographic *c*-axis of the TTB structure were identified in the highly nonstoichiometric $Ba_{0.5-x}TaO_{3-x}$ by electron, synchrotron, and neutron powder diffraction techniques. Regarding the $Ba_{0.22}TaO_{2.72}$ (x = 0.28) composition, the filling of Ba^{2+} and $(TaO)^{3+}$ groups into the pentagonal tunnels is partially ordered along the *ab*-plane of the simple TTB structure, forming the $\sqrt{2}$-type TTB superstructure in P*bmm*. With the Ta/Ba ratio drifting to more Ta_2O_5-rich composition $Ba_{0.175}TaO_{2.675}$ (x = 0.325) with the larger $(TaO)^{3+}$ and less Ba^{2+} contents in the pentagonal tunnels, complete ordering along the *b*-axis of the simple TTB structure occurred, resulting in a triple ordered TTB superstructure crystallizing in $P2_12_12$. In contrast with the linear thermal expansion and normal dielectric behavior of the stoichiometric $Ba_6GaTa_9O_{30}$ showing a monotonic decrease of permittivity with temperature within 100−800 K, these highly nonstoichiometric TTB superstructures as well as slightly nonstoichiometric simple TTB $Ba_{0.4}TaO_{2.9}$ displayed the curvature on the thermal expansion of the *c*-axis around 600 K and abnormally broad and frequency-dependent extrinsic dielectric relaxations (10^3−10^5 Hz) above room temperature. These unusual phenomena are thought to be linked with the common structural feature of the tunnel emptiness in the nonstoichiometric TTB materials, which facilitates the long-range motion of Ba^{2+} cations in the highly nonstoichiometric $(TaO)^{3+}$-containing $Ba_{0.5-x}TaO_{3-x}$ compositions.

ASSOCIATED CONTENT

Supporting Information

The Supporting Information is available free of charge on the ACS Publications website at DOI: 10.1021/acs.inorgchem.5b01098.

Final refined crystallographic parameters and selected bond distances of triple TTB $Ba_{0.175}TaO_{2.675}$; Rietveld fits of SPD and NPD data, final refined structural parameters

DOI: 10.1021/acs.inorgchem.5b01098
Inorg. Chem. 2015, 54, 8978−8986

and interatomic distances for $\sqrt{2}$-type TTB $Ba_{0.22}TaO_{2.72}$ and simple TTB $Ba_6GaTa_9O_{30}$; electron diffraction patterns of $Ba_6GaTa_9O_{30}$ and $Ba_{0.4}TaO_{2.9}$; Rietveld fit of laboratory XRD data, final refined structural parameters, interatomic distances for $Ba_{0.4}TaO_{2.9}$; temperature dependencies of the cell parameters of $\sqrt{2}$-type TTB phase in $Ba_{0.25}TaO_{2.75}$ sample; impedance data analysis of $Ba_{0.5-x}TaO_{3-x}$ TTB oxides (PDF)

Crystallographic information in CIF file for the triple and $\sqrt{2}$-type TTB phases as well as the simple TTB phases of $Ba_6GaTa_9O_{30}$ and $Ba_{0.4}TaO_{2.9}$ (CIF)

AUTHOR INFORMATION

Corresponding Authors

*E-mail: kuangxj@glut.edu.cn (X.K.).

*E-mail: mathieu.allix@cnrs-orleans.fr (M.A.).

Notes

The authors declare no competing financial interest.

ACKNOWLEDGMENTS

The National Natural Science Foundation of China (No. 21101174, 2151130134), Guangxi Natural Science Foundation (No. 2014GXNSFGA118004), Program for New Century Excellent Talents in University (No. NCET-13-0752), and Guangxi Key Laboratory for Advanced Materials and New Preparation Technology (No. 12AA-11) are acknowledged for the financial support. Use of the Advanced Photon Source was supported by the U.S. DOE under Contract No. DE-AC02-06CH11357. We are grateful to Prof. Laijun Liu (Guilin University of Technology) for the valuable discussion on the dielectric relaxation.

REFERENCES

(1) Yamauchi, K.; Picozzi, S. *Phys. Rev. Lett.* **2010**, *105*, 107202.

(2) Chi, E. O.; Gandini, A.; Ok, K. M.; Zhang, L.; Halasyamani, P. S. *Chem. Mater.* **2004**, *16*, 3616−3622.

(3) Zhu, X. L.; Chen, X. M.; Liu, X. Q.; Li, X. G. *J. Appl. Phys.* **2009**, *105*, 124110.

(4) Arnold, D. C.; Morrison, F. D. *J. Mater. Chem.* **2009**, *19*, 6485−6488.

(5) Prades, M.; Masó, N.; Beltrán, H.; Cordoncillo, E.; West, A. R. *Inorg. Chem.* **2013**, *52*, 1729−1736.

(6) Lin, K.; Rong, Y.; Wu, H.; Huang, Q.; You, L.; Ren, Y.; Fan, L.; Chen, J.; Xing, X. *Inorg. Chem.* **2014**, *53*, 9174−9180.

(7) Bonner, W. A.; Grodkiewicz, W. H.; Van Uitert, L. G. *J. Cryst. Growth* **1967**, *1*, 318−319.

(8) Ohsato, H. *J. Eur. Ceram. Soc.* **2007**, *27*, 2911−2915.

(9) Cao, J.; Yu, X. D.; Kuang, X. J.; Su, Q. *Inorg. Chem.* **2012**, *51*, 7788−7793.

(10) Kuang, X.; Pan, F.; Cao, J.; Liang, C.; Suchomel, M. R.; Porcher, F.; Allix, M. *Inorg. Chem.* **2013**, *52*, 13244−13252.

(11) Rietveld, H. M. *J. Appl. Crystallogr.* **1969**, *2*, 65−71.

(12) Coelho, A. A. *TOPAS Academic V4*; Coelho Software: Brisbane, Australia, 2005.

(13) Brown, I. D.; Altermatt, D. *Acta Crystallogr., Sect. B: Struct. Sci.* **1985**, *41*, 244−247.

(14) Boultif, A.; Louer, D. *J. Appl. Crystallogr.* **1991**, *24*, 987−993.

(15) Werner, P. *Z. Kristallogr.* **1964**, *120*, 375−387.

(16) Vanderah, T. A.; Roth, R. S.; Siegrist, T.; Febo, W.; Loezos, J. M.; Wong-Ng, W. *Solid State Sci.* **2003**, *5*, 149−164.

(17) Sleight, A. W. *Acta Chem. Scand.* **1966**, *20*, 1102−1112.

(18) Craig, D. C.; Stephenson, N. C. *J. Solid State Chem.* **1971**, *3*, 89−100.

(19) Stephenson, N. *Acta Crystallogr., Sect. B: Struct. Crystallogr. Cryst. Chem.* **1968**, *24*, 637−653.

(20) Krumeich, F.; Worle, M.; Hussain, A. *J. Solid State Chem.* **2000**, *149*, 428−433.

(21) Lufaso, M. W. *Chem. Mater.* **2004**, *16*, 2148−2156.

(22) Bieringer, M.; Moussa, S. M.; Noailles, L. D.; Burrows, A.; Kiely, C. J.; Rosseinsky, M. J.; Ibberson, R. M. *Chem. Mater.* **2003**, *15*, 586−597.

(23) Mallinson, P. M.; Claridge, J. B.; Rosseinsky, M. J.; Ibberson, R. M.; Wright, J. P.; Fitch, A. N. *Chem. Mater.* **2007**, *19*, 4731−4740.

(24) Levin, I.; Stennett, M. C.; Miles, G. C.; Woodward, D. I.; West, A. R.; Reaney, I. M. *Appl. Phys. Lett.* **2006**, *89*, 122908.

(25) Kang, B. S.; Choi, S. K.; Park, C. H. *J. Appl. Phys.* **2003**, *94*, 1904−1911.

(26) Ang, C.; Yu, Z.; Cross, L. E. *Phys. Rev. B: Condens. Matter Mater. Phys.* **2000**, *62*, 228−236.

DOI: 10.1021/acs.inorgchem.5b01098
Inorg. Chem. 2015, 54, 8978−8986